# Elastic scattering and quasielastic transfer for $^{32}S+^{96,100}Mo$ at $E_{lab}=180$ MeV

D. M. Herrick, F. L. H. Wolfs, D. C. Bryan, C. G. Freeman, K. L. Kurz, D. H. Mathews, P. A. A. Perera, and M. T. Zanni

*Nuclear Structure Research Laboratory, University of Rochester, Rochester, New York 14627*

(Received 14 November 1994)

Cross sections for elastic scattering and quasielastic transfer have been measured for $^{32}S+^{96,100}Mo$ at $E_{lab}=180$ MeV ($\sim$ 60% above the Coulomb barrier). The transfer yields are dominated by the ($^{32}S$,$^{33}S$) and ($^{32}S$,$^{31}P$) reactions which account for about 50% of the total quasielastic transfer strength. The transfer probabilities show an exponential decrease with increasing distance of closest approach. The measured decay constants are smaller than the binding-energy derived decay constants. The observed enhancements of the transfer probabilities for the simplest single-step transfer reactions (involving the transfer of up to two nucleons) can be understood quantitatively in terms of quantum diffraction.

PACS number(s): 25.70.Bc, 25.70.Hi

## I. INTRODUCTION

Nucleon transfer in heavy-ion induced collisions at large internuclear distances has been studied extensively in recent years [1–17]. Nucleon transfer at large internuclear distances is often described in terms of tunneling through a one-dimensional potential barrier. This tunneling picture predicts that the transfer probability decreases exponentially with increasing internuclear distance with a decay constant equal to $\sqrt{2\mu B/\hbar^2}$, where $\mu$ and $B$ are the reduced mass and binding energy of the transferred nucleon or nucleon cluster, respectively. The observed dependence of the one-neutron transfer yields on the internuclear distance is generally in good agreement with the predictions of this semiclassical model. The semiclassical model predicts that the binding-energy derived decay constant for two-neutron transfer is roughly double that for one-neutron transfer. However, the majority of the two-neutron reactions studied show measured decay constants similar to those observed for one-neutron transfer. This observation has become known as the "slope anomaly" [6].

One approach used to study nucleon transfer at large internuclear distances is to measure transfer excitation functions at sub-barrier energies by detecting the target-like recoils at 0°. The internuclear distance can be chosen by selecting the proper bombarding energy. The use of a recoil separator to carry out this type of measurement was pioneered by Pass *et al.* [3]. The advantage of this method is that the nuclear force does not affect the trajectories of the nuclei. However, due to the low energy of the target recoils, complete particle identification is difficult to achieve, and isotopic identification is usually based on distorted-wave Born approximation (DWBA) and/or $Q$-value arguments. The recoil technique has been applied by Roberts *et al.* [15], using the Rochester Recoil Mass Spectrometer, to measure the strength of nucleon transfer for $^{32}S+^{100}Mo$. The measured transfer probabilities for both one- and two-neutron transfer for this system are well described in terms of the simple one-dimensional tunneling model [15].

Another approach used to study nucleon transfer at large internuclear distances is to measure transfer cross sections at angles forward of the grazing angle and at energies above the Coulomb barrier [4,5,9,10,13,14]. In this approach the angular dependence of the distance of closest approach is used to vary the internuclear distance. The advantage of this method is that complete particle identification can be achieved. However, the assumption of Rutherford trajectories becomes questionable, and diffractive scattering effects can become important [10].

We have measured the probability of nucleon transfer at large internuclear distances for $^{32}S+^{96,100}Mo$ at $E_{lab}$ = 180 MeV ($\sim$ 60% above the Coulomb barrier) using the Rochester Enge split-pole spectrograph. This measurement is part of a systematic study to determine the dependence of nucleon transfer yields on $Q$ value, bombarding energy, and neutron number for $^{32}S+^{92,94,95,96,97,98,100}Mo$. The results of our measurement of neutron transfer for $^{32}S+^{100}Mo$ at an energy well above the Coulomb barrier will be compared with the results obtained by Roberts *et al.* at sub-barrier energies [15].

The material presented in this paper is organized in the following way. In Sec. II the experimental details of the measurement are described. The experimental results are discussed in Sec. III. The dependence of the measured transfer probability on the distance of the closest approach is compared with the predicted dependence in Sec. IV. In addition, the effect of quantum diffraction on the measured angular distributions is discussed in detail in Sec. IV. A summary of our conclusions is presented in Sec. V.

## II. EXPERIMENTAL DETAILS

The experiment was performed using a 180 MeV $^{32}S$ beam from the upgraded MP tandem accelerator of the

 

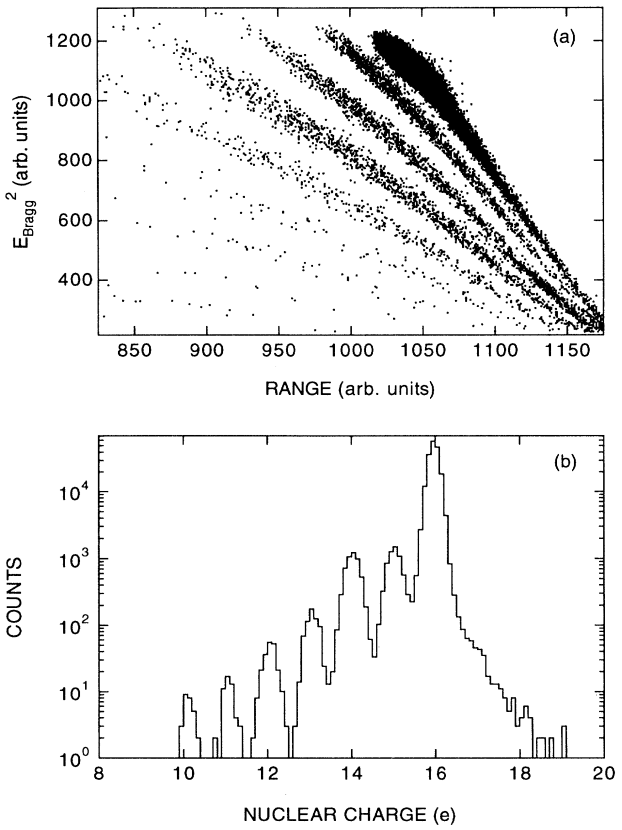


FIG. 1. (a) Square of the measured BCD energy versus the measured range obtained for $^{32}$S+$^{100}$Mo at $\theta_{lab} = 30°$. (b) $Z$ spectrum obtained by linearizing the data shown in (a).

Nuclear Structure Research Laboratory of the University of Rochester. The $^{32}$S ions were incident on $^{96,100}$Mo targets. The thicknesses of these targets were determined by measuring the energy loss of $\alpha$ particles from a $^{241}$Am source and were found to be 320 and 530 $\mu$g/cm$^2$ for $^{96}$Mo and $^{100}$Mo, respectively. The enrichments of the targets used are 96.8% and 95.9% for $^{96}$Mo and $^{100}$Mo, respectively. The main contaminants in the $^{96}$Mo target are $^{95}$Mo (0.9%) and $^{97}$Mo (1.0%). The main contaminant in the $^{100}$Mo target is $^{98}$Mo (1.7%). No corrections for these low levels of contamination were made in the transfer yields obtained with the $^{96,100}$Mo targets.

The reaction products were momentum analyzed using an Enge split-pole spectrograph and detected in the focal plane with a position-sensitive ionization counter [18]. The detector consists of a parallel plate avalanche counter (PPAC) backed by a large Bragg curve detector (BCD). For this experiment, operating pressures were 5.5 Torr of isobutane in the PPAC and 85 Torr of freon in the BCD. The magnetic field of the spectrograph was chosen such that the five most abundant charge states were detected simultaneously in the focal plane. The measured yields were corrected for the fraction of the atomic charge state distribution not detected in the focal plane. This correction was always less than 10%. A silicon surface-barrier detector, mounted at $\theta_{lab} = 15°$, was used for relative normalization between different runs and to monitor variations in beam intensity and target quality. The absolute normalization was obtained using the elastic-scattering data at the forward angles and assuming that these yields are described by Rutherford scattering. The total error in the absolute normalization was estimated to be 15%.

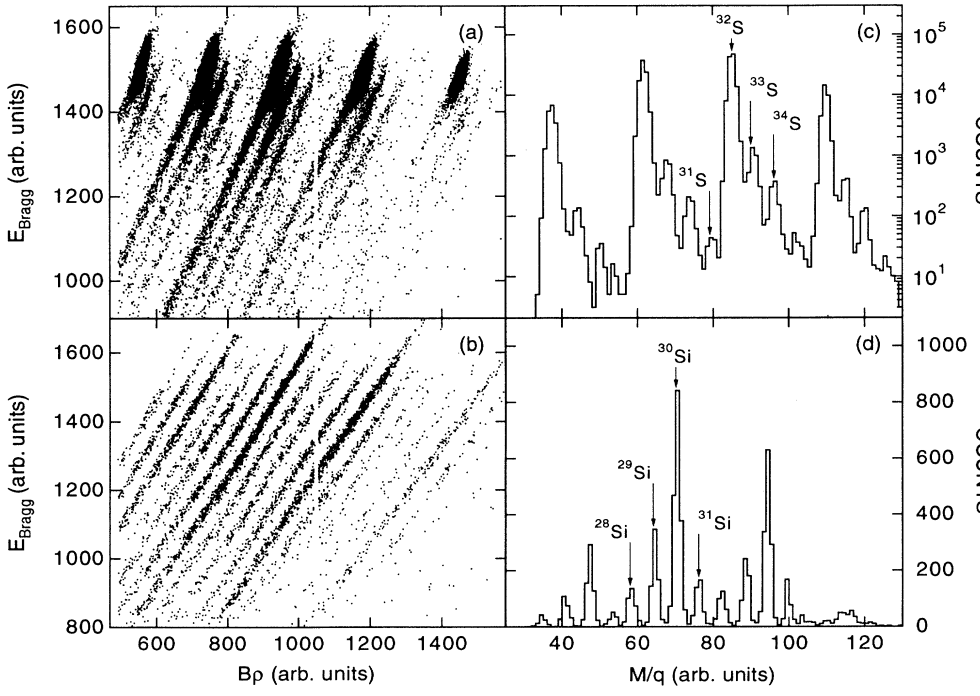


FIG. 2. (a) Measured BCD energy versus the measured focal plane distance for S fragments produced in the $^{32}$S+$^{100}$Mo reaction at $\theta_{lab} = 30°$. (b) Measured BCD energy versus the measured focal plane distance for Si fragments produced in the $^{32}$S +$^{100}$Mo reaction at $\theta_{lab} = 30°$. (c) $M/q$ spectrum obtained by linearizing the data shown in (a). The various S isotopes associated with the strongest atomic charge state are labeled. (d) $M/q$ spectrum obtained by linearizing the data shown in (b). The various Si isotopes associated with the strongest atomic charge state are labeled.

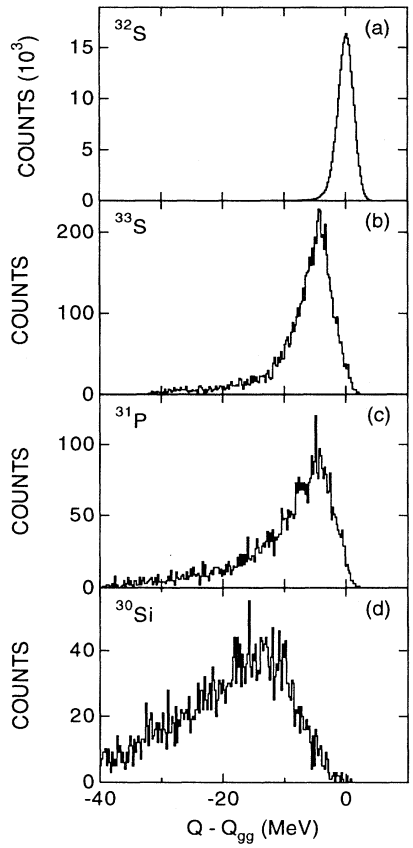


FIG. 3. (a) Energy spectrum of $^{32}$S ions produced in the $^{32}$S+$^{100}$Mo reaction at $\theta_{lab} = 30°$. (b) Energy spectrum of $^{33}$S ions produced in the $^{32}$S+$^{100}$Mo reaction at $\theta_{lab} = 30°$. (c) Energy spectrum of $^{31}$P ions produced in the $^{32}$S+$^{100}$Mo reaction at $\theta_{lab} = 30°$. (d) Energy spectrum of $^{30}$Si ions produced in the $^{32}$S+$^{100}$Mo reaction at $\theta_{lab} = 30°$.

The nuclear charge was obtained from the measured energy and range of the particles in the BCD. Figure 1(a) shows a two-dimensional spectrum of the square of the measured energy versus the range obtained for $^{32}$S+$^{100}$Mo at $\theta_{lab} = 30°$. A $Z$ spectrum obtained by linearizing the data shown in Fig. 1(a) is shown in Fig. 1(b). The $Z$ resolution is $0.3e$ [full width at half maximum (FWHM)]. The mass of the detected particles was determined from the measured energy (BCD) and the measured position along the focal plane (PPAC). Figures 2(a) and 2(b) show two-dimensional spectra of measured energy versus measured position along the focal plane for particles with $Z = 16$ and 14, respectively, obtained for $^{32}$S+$^{100}$Mo at $\theta_{lab} = 30°$. $M/q$ spectra, obtained by linearizing the data shown in Figs. 2(a) and 2(b), are shown in Figs. 2(c) and 2(d), respectively. The mass resolution is 0.3 u (FWHM).

Figure 3 shows energy spectra of $^{32,33}$S, $^{31}$P, and $^{30}$Si ions obtained for $^{32}$S+$^{100}$Mo at $\theta_{lab} = 30°$. The energy resolution obtained is 1.5 MeV (FWHM) and is dominated by energy straggling in the target and in the various foils of the focal-plane detector system. This energy resolution is insufficient to resolve individual states in projectile- and/or targetlike fragments. The quasielastic yields were extracted by summing the energy spectra over a 20 MeV window of excitation energy extending from the ground-state $Q$ value ($|Q - Q_{gg}| \leq 20$ MeV). This range of excitation energies was chosen to reduce the contributions of deep-inelastic scattering to the total transfer yields. The ungated transfer angular distributions can be decomposed into a contribution of Gaussian shape peaking near the grazing angle, and a contribution falling off exponentially with angle. The Gaussian component gets its main contribution from quasielastic reactions ($|Q - Q_{gg}| \leq 20$ MeV) while the exponential component is associated with more inelastic processes. Quasielastic transfer, predominantly to low-lying states in projectilelike and targetlike fragments, is evident in the energy spectra of $^{33}$S and $^{31}$P but not in the energy spectrum of $^{30}$Si where only 50% of the total yield has $|Q - Q_{gg}| \leq 20$ MeV.

## III. EXPERIMENTAL RESULTS

### A. Elastic scattering and the total reaction cross section

The measured elastic-scattering yields (including inelastic excitation with $|Q - Q_{gg}| \leq 20$ MeV) divided by

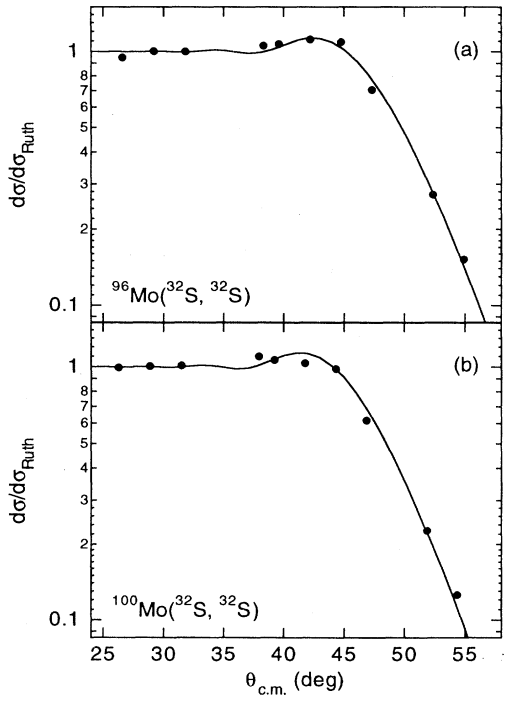


FIG. 4. Elastic-scattering angular distributions, including inelastic excitation with $|Q - Q_{gg}| \leq 20$ MeV, for (a) $^{32}$S+$^{96}$Mo and (b) $^{32}$S+$^{100}$Mo at $E_{lab} = 180$ MeV. The solid curves are results of optical-model calculations used to obtain the total reaction cross sections.

the Rutherford cross section versus the center-of-mass scattering angle for $^{32}$S+$^{96,100}$Mo are shown in Fig. 4. The solid curves in Fig. 4 show the results of optical-model fits to the data using the code PTOLEMY [19] with parameters $V = 100$ MeV, $R_0 = 1.10$ fm, $a = 0.69$ fm, $W = 40$ MeV, $R_{i0} = 1.24$ fm, $a_i = 0.55$ fm, $R_{Co} = 1.4$ fm. The total reaction cross sections obtained from the optical-mode analysis are 1900±280 mb for $^{32}$S+$^{96}$Mo and 1970±300 mb for $^{32}$S+$^{100}$Mo. These values are consistent with the total reaction cross sections obtained from the quarter point angles ($\theta_{1/4}$) of the sum of elastic and inelastic scattering. Using the generalized Fresnel method [20] with a width parameter $\Delta = 4.0\hbar$ the total reaction cross sections from the quarter point angles are 1800 ± 80 mb for $^{32}$S+$^{96}$Mo and 1900±80 mb for $^{32}$S+$^{100}$Mo.

### B. Transfer yields

Figure 5 shows the measured angular distributions of various transfer channels with $|Q - Q_{gg}| \leq 20$ MeV for $^{32}$S+$^{100}$Mo at $E_{lab} = 180$ MeV. The solid and dashed curves show the results of fits to the measured angular distributions with the following function:

$$\frac{d\sigma}{d\Omega} = \left| \frac{1}{2ik} \sum_l (2l+1) a_l e^{2i\sigma_l} P_l(\cos\theta_{c.m.}) \right|^2 , \quad (1)$$

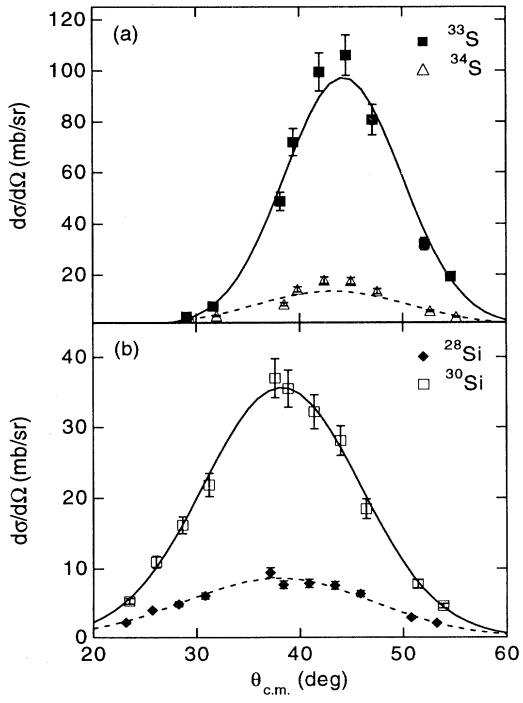


FIG. 5. Measured angular distributions for various quasielastic transfer channels observed for $^{32}$S+$^{100}$Mo at $E_{lab} = 180$ MeV. The solid and dashed curves show the results of fits to the measured angular distributions with Eq. (1).

TABLE I. Ground-state $Q$ values and quasielastic transfer cross sections obtained for $^{32}$S+$^{96}$Mo at $E_{lab} = 180$ MeV. Also shown are the angular momentum parameters of the parametrized form factor, obtained from fits to the measured transfer angular distributions.

| $Z(e)$ | $A$ | $Q_{gg}$(MeV) | $l_0$ | $\Delta l$ | $\sigma_{transfer}$ (mb) |
|---|---|---|---|---|---|
| 16 | 31 | −8.27 | 105.8±0.7 | 6.7±0.2 | 7±1 |
| 16 | 33 | −0.51 | 106.8±0.1 | 10.2±0.1 | 79±12 |
| 16 | 34 | 3.53 | 111.3±0.3 | 8.1±0.1 | 17±2 |
| 15 | 30 | −8.08 | 108.3±0.6 | 6.8±0.2 | 7±1 |
| 15 | 31 | −3.18 | 110.1±0.1 | 9.7±0.1 | 59±9 |
| 15 | 32 | −4.67 | 117.3±0.4 | 7.4±0.1 | 13±2 |
| 15 | 33 | −2.46 | 115.9±0.7 | 6.9±0.2 | 6±1 |
| 14 | 28 | −4.10 | 120.2±0.4 | 6.8±0.1 | 18±3 |
| 14 | 29 | −5.30 | 125.8±0.3 | 6.8±0.1 | 26±4 |
| 14 | 30 | −2.15 | 124.5±0.2 | 7.3±0.1 | 39±6 |
| 14 | 31 | −5.81 | 133.1±0.9 | 5.7±0.2 | 8±1 |

where $k$ is the wave number, $\sigma_l$ is the Coulomb phase shift, $P_l$ is the Legendre polynomial, and $a_l$ is the parametrized form factor. The parametrized form factor was assumed to have a Gaussian distribution centered around $l_0$ and with a width $\Delta l$

$$a_l = f_0 \exp\left\{ -\left( \frac{l - l_0}{\Delta l} \right)^2 \right\} . \quad (2)$$

Tables I and II summarized the optimum values for $l_0$, $\Delta l$, and the angle-integrated transfer yields, obtained from these fits. An interesting note is the occurrence of significant transfer strength in the more complicated channels such as $^{31}$P (one-proton stripping and one-neutron pickup) and $^{31}$Si (two-proton stripping and one-neutron pickup).

Transfer also was observed to channels with $Z < 14e$. However, no attempt was made to obtain absolute cross sections for these channels due to the limited statistics and the uncertainty about the fraction of the atomic charge-state distribution that was detected.

TABLE II. Ground-state $Q$ values and quasielastic transfer cross sections obtained for $^{32}$S+$^{100}$Mo at $E_{lab} = 180$ MeV. Also shown are the angular momentum parameters of the parametrized form factor, obtained from fits to the measured transfer angular distributions.

| $Z(e)$ | $A$ | $Q_{gg}$(MeV) | $l_0$ | $\Delta l$ | $\sigma_{transfer}$ (mb) |
|---|---|---|---|---|---|
| 16 | 31 | −9.70 | 115.7±0.4 | 7.2±0.1 | 7±1 |
| 16 | 33 | 0.36 | 107.6±0.1 | 11.0±0.1 | 105±16 |
| 16 | 34 | 5.84 | 110.8±0.2 | 8.7±0.1 | 21±3 |
| 15 | 30 | −7.40 | 115.3±0.7 | 6.6±0.2 | 6±1 |
| 15 | 31 | −1.44 | 111.7±0.1 | 9.9±0.1 | 64±10 |
| 15 | 32 | −2.05 | 118.4±0.3 | 7.5±0.1 | 19±3 |
| 15 | 33 | 1.47 | 116.4±0.4 | 7.4±0.1 | 8±1 |
| 14 | 28 | −2.61 | 123.2±0.4 | 6.6±0.1 | 13±2 |
| 14 | 29 | −3.05 | 124.5±0.3 | 7.1±0.1 | 23±3 |
| 14 | 30 | 1.33 | 123.7±0.2 | 7.7±0.1 | 46±7 |
| 14 | 31 | −1.30 | 132.6±0.4 | 6.9±0.1 | 12±2 |

## IV. DISCUSSION

### A. Transfer probability

Nucleon transfer at large distances is often described in terms of the transfer probability $P_{\rm tr}$. Different authors have used different definitions to obtain the transfer probability from the differential transfer cross sections $d\sigma_{\rm tr}/d\Omega$. For example, Roberts *et al.* [15] have used

$$P_{\rm tr} = \frac{d\sigma_{\rm tr}/d\Omega}{d\sigma_{\rm el+tr}/d\Omega} , \tag{3}$$

where $d\sigma_{\rm el+tr}/d\Omega$ is the measured cross section for elastic scattering and quasielastic nucleon transfer (including in many cases inelastic excitation of the projectile and/or the targetlike fragments). Pass *et al.* [3] have used

$$P_{\rm tr} = \frac{d\sigma_{\rm tr}/d\Omega}{(1-P_a)d\sigma_{\rm Ruth}/d\Omega} , \tag{4}$$

where $d\sigma_{\rm Ruth}/d\Omega$ is the Rutherford cross section and $P_a$ is the probability that flux is absorbed into any channel other than quasielastic. In this work we have defined the transfer probability as

$$P_{\rm tr} = \frac{d\sigma_{\rm tr}/d\Omega}{2\pi b\, db} , \tag{5}$$

where $d\sigma_{\rm tr}$ is the transfer cross section at a given center-of-mass scattering angle $\theta_{\rm c.m.}$ and $b$ is the impact parameter associated with this scattering angle. Assuming Rutherford trajectories we can rewrite $b\,db$ as

$$b\,db = \frac{\eta}{k\,\sin(\theta_{\rm c.m.}/2)} dD , \tag{6}$$

where $k$ is the wave number, $\eta$ is the Sommerfeld parameter, and $D$ is the distance of closest approach corresponding to a center-of-mass scattering angle $\theta_{\rm c.m.}$. Combining Eq. (5) and Eq. (6) we obtain

$$\frac{P_{\rm tr}}{\sin(\theta_{\rm c.m.}/2)} = \frac{k}{2\pi\eta}\frac{d\sigma_{\rm tr}}{dD} . \tag{7}$$

The differential cross section $d\sigma_{\rm tr}/dD$ can be obtained from the differential cross section $d\sigma_{\rm tr}/d\Omega$ in the following manner:

$$\frac{d\sigma_{\rm tr}}{dD} = \frac{8\pi k}{\eta}\sin^3(\theta_{\rm c.m.}/2)\frac{d\sigma_{\rm tr}}{d\Omega} . \tag{8}$$

The semiclassical model of nucleon transfer at large interaction distances described by Bass [21] predicts that for neutron transfer

$$\frac{P_{\rm tr}}{\sin(\theta_{\rm c.m.}/2)} = \frac{\pi\kappa}{2\eta k} C e^{-2\kappa D} , \tag{9}$$

where $\kappa$ is the binding-energy derived decay constant $\sqrt{2\mu B/\hbar^2}$ and $C$ is a dimensionless factor which is independent of energy and contains mainly spectroscopic information. Note that the right-hand side of Eq. (9) is independent of energy. Therefore, a universal dependence on $D$ is expected for the quantity $P_{\rm tr}/\sin(\theta_{\rm c.m.}/2)$ which was nicely demonstrated by Wirth *et al.* [1] for $^{238}$U+$^{238}$U at laboratory energies between 5.05 MeV/u and 6.07 MeV/u.

The semiclassical model for nucleon transfer is only valid in the region where the influence of the nuclear potential is small. Several authors [1,14,22] have carried out detailed studies of the elastic-scattering angular distributions and determined where the nuclear force becomes important. The conclusions of these studies are that for light systems (like O+Mo, Si+Pb, S+Mo) the absorptive processes set in at distances smaller than $1.65(A_p^{1/3} + A_t^{1/3})$ fm. Therefore, we will compare the transfer yields obtained at scattering angles corresponding to a distance of closest approach larger than $1.65(A_p^{1/3}+A_t^{1/3})$ fm with the predictions of the semiclassical model. The distance of closest approach for elastic scattering is obtained from the center-of-mass scattering angle $\theta_{\rm c.m.}$ according to

$$D = \frac{Z_p Z_t e^2}{2E_{\rm c.m.}}\left(1+\frac{1}{\sin(\theta_{\rm c.m.}/2)}\right) , \tag{10}$$

where $Z_p$ and $Z_t$ are the nuclear charges of the projectile

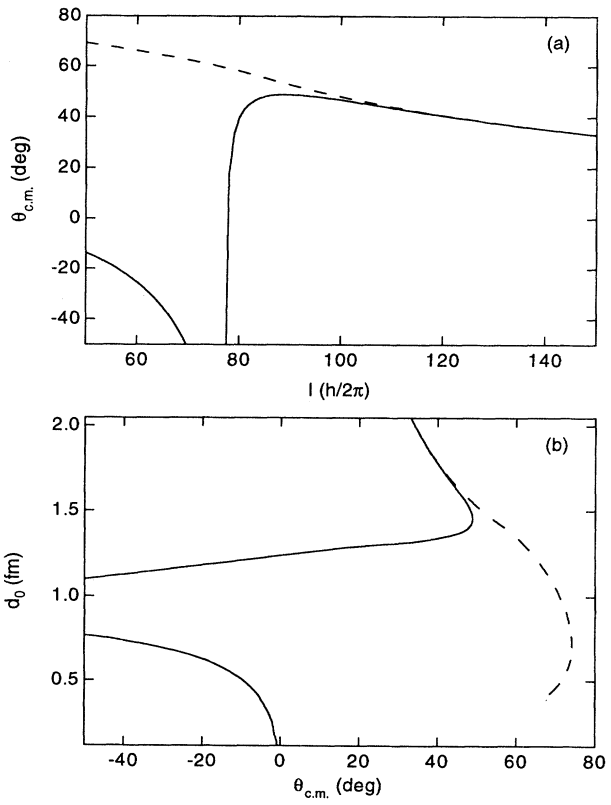


FIG. 6. Results of classical trajectory calculations for $^{32}$S+$^{100}$Mo at $E_{\rm lab}$ = 180 MeV under the influence of only the Coulomb potential (dashed lines) and under the influence of both the Coulomb and the real nuclear potential (solid lines).

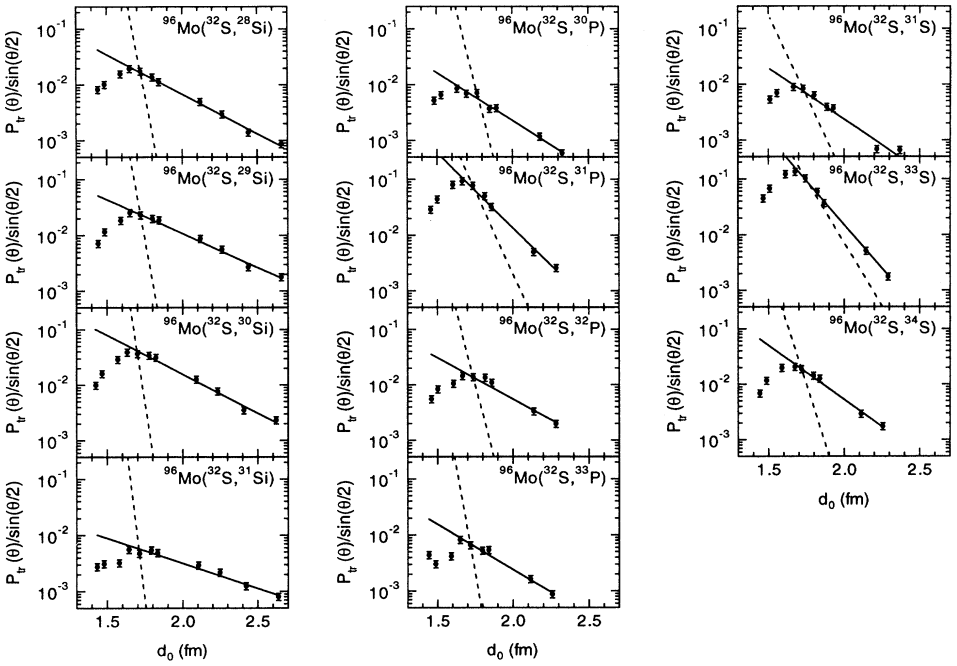


FIG. 7. Transfer probability, divided by $\sin(\theta_{\rm c.m.}/2)$, for various quasielastic transfer channels observed for $^{32}$S+$^{96}$Mo at $E_{\rm lab}$ = 180 MeV. The solid lines show the results of exponential fits to the data at $d_0 > 1.65$ fm. The dashed lines have slopes that are consistent with the binding-energy derived decay constants for the various transfer channels.

and target, respectively, and $E_{\rm c.m.}$ is the center-of-mass energy. For transfer reactions the Rutherford trajectories of the incoming and outgoing channels can be very different, especially in the case of charge transfer, and Eq. (10) does not apply. The distance of closest approach $D_i$ associated with the incoming channel is equal to

$$D_i = \frac{Z_p Z_t e^2}{2E_{\rm c.m.i}}\left(1+\frac{1}{\sin(\theta_{\rm c.m.i}/2)}\right), \qquad (11)$$

where $E_{\rm c.m.i}$ is the center-of-mass energy of the incoming channel and $\theta_{\rm c.m.i}$ is the center-of-mass scattering angle associated with the incoming Rutherford trajectory. The distance of closest approach $D_f$ associated with the outgoing channel is equal to

$$D_f = \frac{(Z_p \pm z)(Z_t \mp z)e^2}{2E_{\rm c.m.f}}\left(1+\frac{1}{\sin(\theta_{\rm c.m.f}/2)}\right), \qquad (12)$$

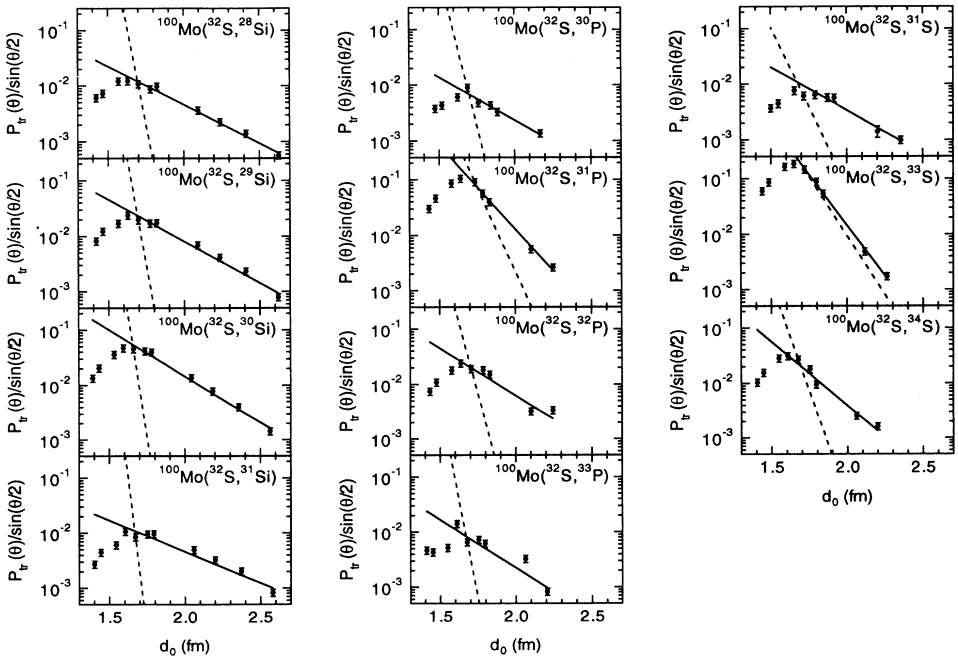


FIG. 8. Transfer probability, divided by $\sin(\theta_{\rm c.m.}/2)$, for various quasielastic transfer channels observed for $^{32}$S+$^{100}$Mo at $E_{\rm lab}$ = 180 MeV. The solid lines show the results of exponential fits to the data at $d_0 > 1.65$ fm. The dashed lines have slopes that are consistent with the binding-energy derived decay constants for the various transfer channels.

where $E_{c,m,f}$ is the center-of-mass energy of the outgoing channel, $\theta_{c.m.f}$ is the center-of-mass scattering angle associated with the outgoing Rutherford trajectory, and $z$ is the nuclear charge of the transferred nucleon or nucleon cluster. Requiring that the incoming and outgoing trajectories are matched at the distance of closest approach, that is $D = D_i = D_f$, we can obtain $D$ from Eqs. (11) and (12) by requiring that $\theta_{c.m.} = (\theta_{c.m.i}/2 + \theta_{c.m.f}/2)$.

Figure 6(a) shows the calculated deflection function for $^{32}$S+$^{100}$Mo at $E_{lab}$ = 180 MeV. Figure 6(b) shows the calculated distance of closest approach divided by $(A_p^{1/3} + A_t^{1/3})$ as a function of the center-of-mass scattering angle. The dashed curves are obtained if only the Coulomb potential is present. The solid curves show the effect of including the real nuclear potential obtained from the optical-model fits of the elastic- and inelastic-scattering angular distributions. Beyond a distance of closest approach of 1.65 $(A_p^{1/3} + A_t^{1/3})$ fm the effect of the nuclear potential on the trajectories can be neglected. This critical distance corresponds to a center-of-mass scattering angle of 45°. However, Fig. 6(a) illustrates that even in this classical picture several different partial waves contribute to the yield observed at $\theta_{c.m.} \leq 45°$.

### B. Transfer probabilities for $^{32}$S+$^{96,100}$Mo

The measured differential cross sections for the various transfer channels observed for $^{32}$S+$^{96,100}$Mo at $E_{lab}$ = 180 MeV have been converted to transfer probabilities using Eqs. (7) and (8). The distance of closest approach has been calculated at each angle using the procedure discussed in Sec. IV A, even though this equation only provides a realistic distance of closest approach for $\theta_{c.m.} \leq 45°$. The extracted transfer probabilities, divided by $\sin(\theta_{c.m.}/2)$, are shown in Figs. 7 and 8 as a function of $d_0 = D/(A_p^{1/3} + A_t^{1/3})$ fm for the various transfer channels observed. The solid lines in Figs. 7 and 8 show the results of fits to the data at $d_0 > 1.65$ fm with Eq. (9). The decay constants extracted from these fits are listed in Tables III and IV. The dashed lines in Figs. 7 and 8

TABLE III. Measured decay constants ($\kappa_{measured}$) obtained from the measured transfer probabilities for $^{32}$S+$^{96}$Mo at $E_{lab}$ = 180 MeV. Also listed are the decay constants calculated on the basis of the binding energy ($\kappa_{theory}$).

| | $\kappa_{measured}$ (fm$^{-1}$) | $\kappa_{theory}$ (fm$^{-1}$) |
|---|---|---|
| $^{96}$Mo($^{32}$S,$^{31}$S) | 0.27±0.01 | 0.86 |
| $^{96}$Mo($^{32}$S,$^{33}$S) | 0.48±0.01 | 0.67 |
| $^{96}$Mo($^{32}$S,$^{34}$S) | 0.30±0.01 | 1.27 |
| $^{96}$Mo($^{32}$S,$^{30}$P) | 0.22±0.03 | 1.61 |
| $^{96}$Mo($^{32}$S,$^{31}$P) | 0.44±0.02 | 0.89 |
| $^{96}$Mo($^{32}$S,$^{32}$P) | 0.25±0.02 | 1.57 |
| $^{96}$Mo($^{32}$S,$^{33}$P) | 0.26±0.02 | 2.19 |
| $^{96}$Mo($^{32}$S,$^{28}$Si) | 0.20±0.01 | 2.09 |
| $^{96}$Mo($^{32}$S,$^{29}$Si) | 0.22±0.01 | 2.24 |
| $^{96}$Mo($^{32}$S,$^{30}$Si) | 0.25±0.01 | 2.61 |
| $^{96}$Mo($^{32}$S,$^{31}$Si) | 0.17±0.01 | 3.32 |

TABLE IV. Measured decay constants ($\kappa_{measured}$) obtained from the measured transfer probabilities for $^{32}$S+$^{100}$Mo at $E_{lab}$ = 180 MeV. Also listed are the decay constants calculated on the basis of the binding energy ($\kappa_{theory}$) and the decay constants obtained by Roberts *et al.* [15] at subbarrier energies ($\kappa_{Roberts}$).

| | $\kappa_{measured}$ (fm$^{-1}$) | $\kappa_{theory}$ (fm$^{-1}$) | $\kappa_{Roberts}$ (fm$^{-1}$) |
|---|---|---|---|
| $^{100}$Mo($^{32}$S,$^{31}$S) | 0.23±0.02 | 0.84 | |
| $^{100}$Mo($^{32}$S,$^{33}$S) | 0.54±0.02 | 0.63 | 0.66±0.02 |
| $^{100}$Mo($^{32}$S,$^{34}$S) | 0.34±0.03 | 1.16 | 0.99±0.14 |
| $^{100}$Mo($^{32}$S,$^{30}$P) | 0.22±0.03 | 1.61 | |
| $^{100}$Mo($^{32}$S,$^{31}$P) | 0.44±0.02 | 0.89 | |
| $^{100}$Mo($^{32}$S,$^{32}$P) | 0.25±0.02 | 1.53 | |
| $^{100}$Mo($^{32}$S,$^{33}$P) | 0.26±0.02 | 2.10 | |
| $^{100}$Mo($^{32}$S,$^{28}$Si) | 0.20±0.01 | 2.08 | |
| $^{100}$Mo($^{32}$S,$^{29}$Si) | 0.22±0.01 | 2.24 | |
| $^{100}$Mo($^{32}$S,$^{30}$Si) | 0.25±0.01 | 2.61 | |
| $^{100}$Mo($^{32}$S,$^{31}$Si) | 0.17±0.01 | 3.28 | |

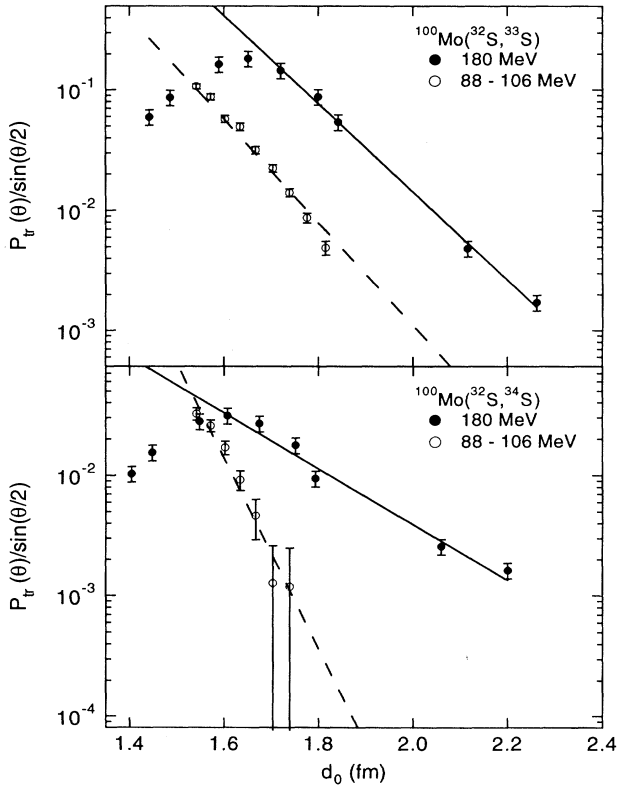


FIG. 9. Comparison between the neutron transfer probabilities obtained for $^{32}$S+$^{100}$Mo at energies below the Coulomb barrier [15] and at $E_{lab}$ = 180 MeV. The dashed lines have slopes that are consistent with the binding-energy derived decay constants for the various transfer channels (normalized to the subbarrier data). The solid lines show fits to the data obtained at $E_{lab}$ = 180 MeV.

have slopes that are given by the binding-energy derived decay constants for the various transfer channels.

Figure 9 shows the neutron transfer probabilities obtained in the current experiment for $^{32}$S+$^{100}$Mo and those obtained by Roberts *et al.* [15] at energies below the Coulomb barrier. It should be noted that the data obtained by Roberts *et al.* did not provide nuclear charge information, and particle identification was inferred on the basis of $Q$-value arguments and DWBA calculations. These suggest that at energies below the Coulomb barrier the $^{100}$Mo($^{32}$S, $A = 33$) and $^{100}$Mo($^{32}$S, $A = 34$) reactions are dominated by neutron transfer while the $^{100}$Mo($^{32}$S, $A = 31$) reaction is dominated by proton transfer. The data obtained at energies below the Coulomb barrier have decay constants that are close to those expected theoretically. The data obtained for $^{100}$Mo($^{32}$S, $^{34}$S) at $E_{\rm lab} = 180$ MeV suggest a decay constant that is significantly smaller than the decay constant associated with the data obtained below the Coulomb barrier. For the $^{100}$Mo($^{32}$S,$^{33}$S) reaction the decay constants of $0.54\pm0.02$ fm$^{-1}$ and $0.66 \pm 0.02$ fm$^{-1}$ obtained at energies above and below the Coulomb barrier, respectively, are in reasonable agreement with the binding-energy derived value of 0.63 fm$^{-1}$. However, the magnitude of the transfer probability at a given distance of closest approach is about an order of magnitude larger at 180 MeV than it is at energies below the Coulomb barrier. This difference in magnitude already suggests a breakdown of the classical model since Eq. (9) predicts

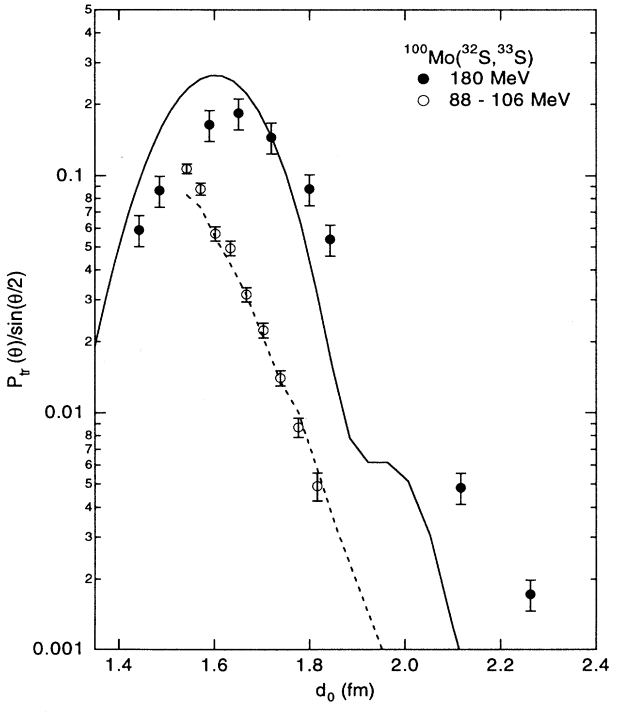


FIG. 10. Comparison between the one-neutron transfer probabilities obtained for $^{32}$S+$^{100}$Mo at energies below the Coulomb barrier [15] and at $E_{\rm lab} = 180$ MeV. The dashed and solid curves show the results of DWBA calculations discussed in the text.

that $P_{\rm tr}/\sin(\theta_{\rm c.m.}/2)$ has a universal dependence on $D$, independent of energy.

The increase in the magnitude of the transfer probability at energies well above the Coulomb barrier is consistent with predictions made on the basis of DWBA calculations. This is illustrated in Fig. 10 which shows the results of DWBA calculations with the code PTOLEMY [19] for the $^{100}$Mo($^{32}$S, $^{33}$S*)$^{99}$Mo* reaction. In the calculation we have assumed that $^{33}$S* is excited to its $3/2^-$ state at 3.220 MeV while $^{99}$Mo* is excited to its $5/2^+$ state at 0.099 MeV. These states were chosen because of their large spectroscopic factors [23,24]. The potential used in these calculations is the optical-model potential obtained from fits to the elastic-scattering angular distributions described in Sec. III A. The dashed curve shows the transfer probability, obtained from the calculated differential transfer cross section at $\theta_{\rm c.m.} = 180°$ at bombarding energies between 80 and 110 MeV, as a function of $d_0$. The calculated transfer probabilities have been normalized to the data from Roberts *et al.* [15]. The solid curve shows the transfer probability obtained from the calculated transfer angular distribution, multiplied by the same normalization constant as was used for the low-energy data. The calculated transfer probabilities decrease significantly faster with increasing $d_0$ than the measured transfer probabilities. Nevertheless, the calculated transfer probability at a given distance of closest approach is significantly larger at 180 MeV than it is at the corresponding sub-barrier energy.

Liang *et al.* have measured the transfer cross sections for the $^{32}$S+$^{100}$Mo system at several energies in the vicinity of the Coulomb barrier [16]. The transfer probabilities for one- and two-neutron pickup, extracted from their measured angular distributions at $E_{\rm lab} = 116$ MeV ($E/V_{\rm Coulomb} = 1.02$), are consistent with the transfer probabilities obtained by Roberts *et al.* [15] at energies well below the barrier, indicating that the expected universal dependence on $D$ of $P_{\rm tr}/\sin(\theta_{\rm c.m.}/2)$, independent of energy, holds at least up to energies in the vicinity of the Coulomb barrier. The transfer probabilities for one- and two-proton stripping, extracted by Liang *et al.* from their measured angular distributions at $E_{\rm lab} = 116$ MeV ($E/V_{\rm Coulomb} = 1.02$), are more than one order of magnitude smaller than the transfer probability obtained in this work. Again, the increase in the magnitude of the transfer probability at energies well above the Coulomb barrier is consistent with predictions made on the basis of DWBA calculations.

### C. Semiclassical interpretation of transfer probabilities

The measured transfer probabilities for the various transfer channels observed in this work all show an exponential fall off at large internuclear distances. The decay constants, obtained by fitting an exponential function to $P_{\rm tr}/\sin(\theta_{\rm c.m.}/2)$ at distances for which $d_0 \geq 1.65$ fm, are listed in Tables III and IV. The resulting fits are shown by the solid lines in Figs. 7 and 8. The dashed lines in Figs. 7 and 8 show the theoretical de-

pendence of $P_{tr}/\sin(\theta_{c.m.}/2)$ on $d_0$, normalized to the data at $d_0 = 1.65$ fm. The slopes are calculated under the assumption that those transfer channels involving the transfer of a single nucleon or a single bound nucleon cluster occur as single-step processes, while the other transfer channels occur as multiple step processes. For this latter group the binding-energy derived decay constants are taken to be the sum of the calculated decay constants of the individual steps. For all transfer channels observed the measured decay constants are smaller than their predicted values.

Wuosmaa *et al.* [10] have suggested that for $^{36}S+^{92}Mo$ two-nucleon transfer at energies well above the barrier is dominated by quantum diffraction due to very localized form factors. The critical angular momentum width $\Delta l_{cr}$ is given by

$$\Delta l_{cr} = \eta \csc\left(\frac{1}{2}\theta_0\right) , \tag{13}$$

where $\theta_0$ is the centroid of the measured angular distribution. For $\Delta l \ll \Delta l_{cr}$ the width of the grazing peak is mainly due to quantum diffraction whereas for $\Delta l \gg \Delta l_{cr}$ it is mainly due to classical deflection. For $^{32}S+^{96,100}Mo$ at $E_{lab} = 180$ MeV the critical angular momentum width is about $14\hbar$. The measured angular momentum widths

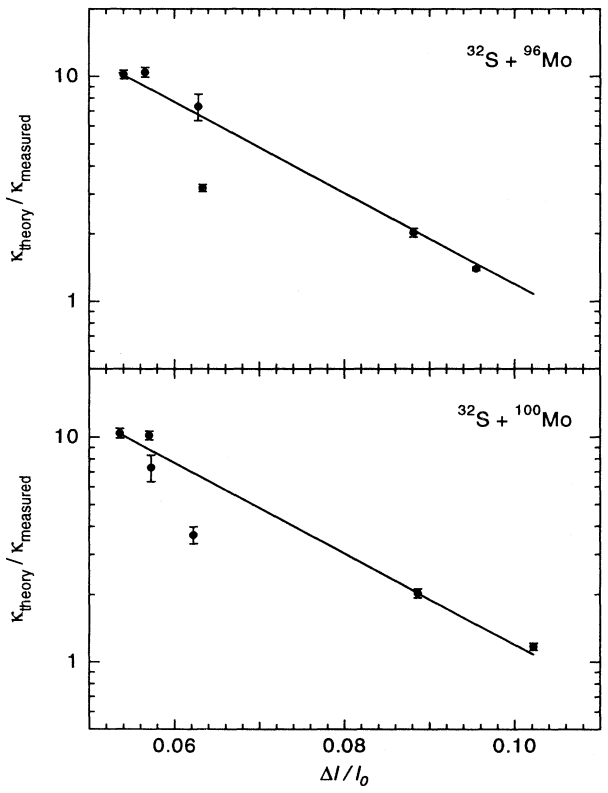


FIG. 11. Ratio of the binding-energy derived decay constants and the measured decay constants for (a) $^{32}S+^{96}Mo$ and (b) $^{32}S+^{100}Mo$ as a function of the width of the angular momentum distribution. The solid lines show the results of a single exponential fit to the data for both systems.

$\Delta l$ for the various transfer channels, listed in Tables I and II, are all smaller than $\Delta l_{cr}$ indicating that quantum diffraction affects the widths of all of the measured angular distributions.

The ratio of the binding-energy derived and the measured decay constants for those transfer reactions that involve the transfer of a single nucleon or a bound nucleon cluster is shown as a function of the relative width of the angular momentum distribution ($\Delta l/l_0$) in Fig. 11. This ratio shows a strong dependence on the relative width of the angular momentum distribution. The data for both systems can be described by the same exponential function, as is illustrated by the solid lines in Fig. 11.

The effect of quantum diffraction on the measured transfer probabilities can be investigated quantitatively by using the semiclassical model developed by Harney, Braun-Munzinger, and Gelbke [25]. Harney, Braun-Munzinger, and Gelbke showed that the measured width of the transfer angular distribution ($\Delta\theta_{tot}$), which is directly related to the decay constant of the transfer probability, is equal to

$$\Delta\theta_{tot} = \sqrt{\Delta\theta_{dif}^2 + \Delta\theta_{clas}^2} , \tag{14}$$

where $\Delta\theta_{clas}$ is the width of the classical angular distribution and $\Delta\theta_{dif}$ is the quantum mechanical contribution to the width of these distributions. Equation (14) shows that these diffractive effects increase the width of the measured angular distribution, and consequently, reduce the deduced decay constant of the transfer probability.

Assuming that the derivative of the deflection function $d\theta_{c.m.}/dl$ is independent of $l$, one can estimate the width of the classical component of the angular distribution ($\Delta\theta_{clas}$) using the experimentally determined value of $\Delta l$,

$$\Delta\theta_{clas} = \left|\frac{d\theta}{dl}\right| \Delta l . \tag{15}$$

Note that $\Delta l$ is obtained by fitting the measured angular distribution with Eq. (1), and its value therefore does not rely on the validity of any classical model. The width of the classical component of the angular distribution, $\Delta\theta_{clas}$, can be used to construct the classical angular distribution $(d\sigma/d\Omega)_{clas}$,

$$\left(\frac{d\sigma}{d\Omega}\right)_{clas}(\theta_{c.m.}) = N \exp\left[-\left(\frac{\theta_{c.m.} - \theta_0}{\Delta\theta_{clas}}\right)^2\right] , \tag{16}$$

where $\theta_0$ is the scattering angle associated with the maximum of the measured angular distribution and $N$ is the differential cross section at $\theta_{c.m.} = \theta_0$. The effect of quantum diffraction on the measured transfer cross sections can be removed by converting the measured transfer cross sections to classical transfer cross sections:

$$\left(\frac{d\sigma}{d\Omega}\right)_{clas} = \frac{\exp\left[-\left(\frac{\theta_{c.m.}-\theta_0}{\Delta\theta_{clas}}\right)^2\right]}{\exp\left[-\left(\frac{\theta_{c.m.}-\theta_0}{\Delta\theta_{tot}}\right)^2\right]} \left(\frac{d\sigma}{d\Omega}\right)_{measured} . \tag{17}$$

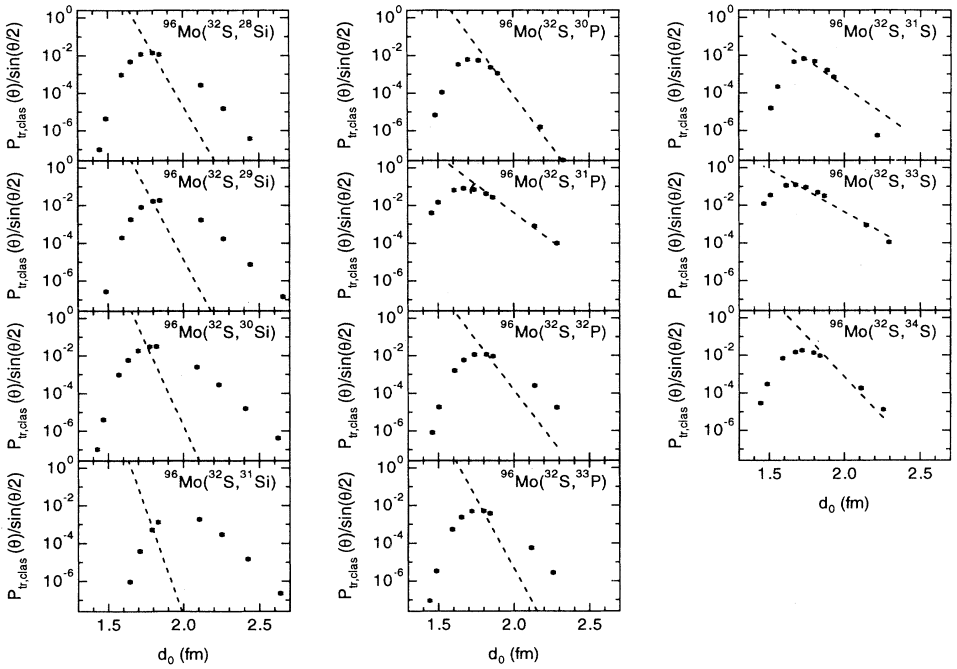


FIG. 12. Transfer probability obtained from the classical angular distributions, divided by $\sin(\theta_{\rm c.m.}/2)$, for various quasielastic transfer channels observed for $^{32}$S+$^{96}$Mo at $E_{\rm lab}$ = 180 MeV. The dashed lines have slopes that are consistent with the binding-energy derived decay constants for the various transfer channels.

The classical angular distribution can be converted to a classical transfer probability, $P_{\rm tr,clas}$, using Eqs. (7) and (8). The resulting classical transfer probabilities are shown as a function of $d_0$ in Figs. 12 and 13. The dashed lines in these figures have slopes that are given by the binding-energy derived decay constants. For the neutron transfer channels the slope of the experimentally deduced classical transfer probability is in reasonable agreement with the binding-energy derived decay constants. The measured decay constants for the ($^{32}$S,$^{30}$P) and ($^{32}$S, $^{31}$P) reactions, which can be considered to be single-step reactions, are in good agreement with the binding-energy derived decay constants. However, for the ($^{32}$S, $^{32}$P) and ($^{32}$S,$^{33}$P) reactions, which are multiple-step processes, the measured decay constants are smaller than the binding-energy derived decay constants. For the reactions producing the various Si isotopes, the measured decay constants are also smaller than the binding-energy

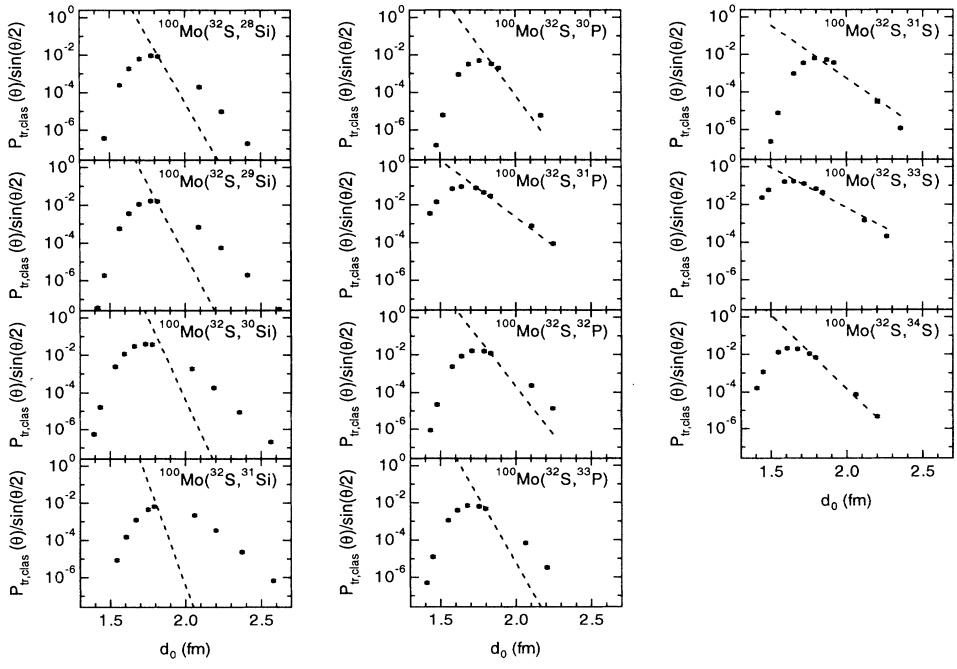


FIG. 13. Transfer probability obtained from the classical angular distributions, divided by $\sin(\theta_{\rm c.m.}/2)$, for various quasielastic transfer channels observed for $^{32}$S+$^{100}$Mo at $E_{\rm lab}$ = 180 MeV. The dashed lines have slopes that are consistent with the binding-energy derived decay constants for the various transfer channels.

derived decay constants. These observations suggest that the slope enhancements observed for simplest single-step transfer reactions (involving the transfer of up to two nucleons) can be understood quantitatively in terms of quantum diffraction. Enhancements are still observed for those reactions that require a multiple-step process. The enhancements observed for the various ($^{32}$S,Si) reactions might indicate that these are multiple-step processes, instead of a single-step transfer of, for example, $^{3}$He and $^{4}$He.

## V. SUMMARY

Cross sections for elastic scattering and quasielastic transfer have been measured for $^{32}$S+$^{96,100}$Mo at $E_{\rm lab}$=180 MeV. The angle-integrated quasielastic transfer yields for the production of various S, P, and Si isotopes are 280±40 mb for $^{32}$S+$^{96}$Mo and 325±50 mb for $^{32}$S+$^{100}$Mo. This corresponds to 15% and 17% of the total reaction cross section for $^{32}$S+$^{96}$Mo and $^{32}$S+$^{100}$Mo, respectively. The transfer yields are dominated by the ($^{32}$S, $^{33}$S) and ($^{33}$S, $^{31}$P) reactions which account for about 50% of the total quasielastic transfer strength.

The measured differential transfer cross sections have been converted into transfer probabilities. These transfer probabilities show an exponential decrease with increasing distance of closest approach. The measured decay constants of the transfer probability are smaller than the binding-energy derived decay constants. It has been shown that the observed enhancements of the decay constants for the simplest single-step transfer reactions (involving the transfer of up to two nucleons) can be understood quantitatively in terms of quantum diffraction. Enhancements observed for those reactions that require a multiple-step process cannot be accounted for in terms of the simple diffraction model discussed here.

## ACKNOWLEDGMENTS

We express our gratitude to the accelerator crew of the NSRL tandem accelerator for providing us with $^{32}$S beams of excellent quality. We also appreciate the many comments we received from Dr. Stuart Gazes on the first draft of this manuscript. This work was supported by a grant from the National Science Foundation.

[1] G. Wirth, W. Brüchle, M. Brügger, F. Wo, K. Sümmerer, F. Funke, J. V. Kratz, M. Lerch, and N. Trautmann, Phys. Lett. B **177**, 282 (1986).
[2] W. v. Oertzen, H. G. Bohlen, B. Gebauer, R. Künkel, F. Pühlhofer, and D. Schüll, Z. Phys. A **326**, 463 (1987).
[3] C. N. Pass, P. M. Evans, A. E. Smith, L. Stuttge, R. R. Betts, J. S. Lilley, D. W. Banes, K. A. Connell, J. Simpson, J. R. Smith, A. N. James, and B. R. Fulton, Nucl. Phys. **A499**, 173 (1989).
[4] L. Corradi, S. J. Skorka, U. Lenz, K. E. G. Löbner, P. R. Pascholati, U. Quade, K. Rudolph, W. Schomburg, M. Steinmayer, H. G. Thies, G. Montagnoli, D. R. Napoli, A. M. Stefanini, A. Tivelli, S. Beghini, F. Scarlassara, C. Signorini, and F. Soramel, Z. Phys. A **334**, 55 (1990).
[5] R. Künkel, W. v. Oertzen, H. G. Bohlen, B. Gebauer, H. A. Bösser, B. Kohlmeyer, J. Speer, F. Pühlhofer, and D. Schüll, Z. Phys. A **336**, 71 (1990).
[6] C. Y. Wu, W. v. Oertzen, D. Cline, and M. W. Guidry, Ann. Rev. Nucl. Part. Sci. **40**, 285 (1990).
[7] H. J. Kim, J. G. d. Campo, D. Shapiro, P. H. Stelson, and D. Napoli, Phys. Rev. C **43**, 1321 (1991).
[8] K. E. Rehm, Ann. Rev. Nucl. Part. Sci. **41**, 429 (1991).
[9] F. Scarlassara, S. Beghini, F. Soramel, C. Signorini, L. Corradi, G. Montagnoli, D. R. Napoli, A. M. Stefanini, and Z. C. Li, Z. Phys. A **338**, 171 (1991).
[10] A. H. Wuosmaa, K. E. Rehm, B. G. Glagola, T. Happ, W. Kutschera, and F. L. H. Wolfs, Phys. Lett. B **255**, 316 (1991).
[11] J. O. F. Niello, J. E. Testoni, M. d. Tada, A. J. Pacheco, D. R. Napoli, A. M. Stefanini, L. Corradi, B. Million, M. Narayanasamy, P. Spolaore, S. Beghini, G. Montagnoli, F. Scarlassara, G. F. Segato, C. Signorini, and F. Soramel, Phys. Rev. C **45**, 748 (1992).
[12] L. Corradi, S. J. Skorka, T. Winkelmann, K. Balog, P. Jänker, H. Leitz, U. Lenz, K. E. G. Löbner, K. Rudolph, M. Steinmayer, H. G. Thies, B. Million, D. R. Napoli, A. M. Stefanini, S. Beghini, G. Montagnoli, F. Scarlassara, C. Signorini, and F. Soramel, Z. Phys. A **346**, 217 (1993).
[13] J. F. Liang, L. L. Lee, J. C. Mahon, and R. J. Vojtech, Phys. Rev. C **47**, R1342 (1993).
[14] K. E. Rehm, B. G. Glagola, W. Kutschera, F. L. H. Wolfs, and A. H. Wuosmaa, Phys. Rev. C **47**, 2731 (1993).
[15] R. B. Roberts, S. B. Gazes, J. E. Mason, M. Satteson, S. G. Teichmann, L. L. Lee, J. F. Liang, J. C. Mahon, and R. J. Vojtech, Phys. Rev. C **47**, R1831 (1993).
[16] J. F. Liang, J. L. L. Lee, J. C. Mahon, and R. J. Vojtech, Phys. Rev. C **50**, 1550 (1994).
[17] C. V. K. Baba, V. M. Datar, K. E. G. Löbner, A. Navin, and F. J. Schindler, Phys. Lett. B **338**, 147 (1994).
[18] F. L. H. Wolfs, D. C. Bryan, K. L. Kurz, D. M. Herrick, P. A. A. Perera, and C. A. White, Nucl. Instrum. Methods A **317**, 221 (1992).
[19] M. H. Macfarlane and S. C. Pieper, "Ptolemy: A Program for Heavy-ion Direct-reaction Calculations," Tech. Rep. ANL-76-11 Rev. 1, Argonne Natl. Lab, IL, 1978 (unpublished).
[20] W. E. Frahn, Nucl. Phys. **A302**, 267 (1978).
[21] R. Bass, *Nuclear Reactions with Heavy Ions* (Springer-Verlag, Berlin, 1980).
[22] Y. T. Oganessian, Y. E. Penionzhkevich, V. I. Man'ko, and V. N. Polyansky, Nucl. Phys. **A303**, 259 (1978).
[23] P. M. Endt, Nucl. Phys. **A521**, 1 (1990).
[24] H.-W. Müller and D. Chmielewska, Nucl. Data Sheets **48**, 663 (1986).
[25] H. L. Harney, P. Braun-Munzinger, and C. K. Gelbke, Z. Phys. **269**, 339 (1974).